Magnetic Resonance Elastography of the Brain using Multi-Shot Spiral Readouts with Self-Navigated Motion Correction

Curtis L. Johnson[1,2], **Matthew D. J. McGarry**[3], **Elijah E. W. Van Houten**[4], **John B. Weaver**[3,5], **Keith D. Paulsen**[3,6], **Bradley P. Sutton**[2,7], and **John G. Georgiadis**[1,2]

[1]Department of Mechanical Science and Engineering, University of Illinois at Urbana-Champaign, Urbana, IL 61801, USA

[2]Beckman Institute for Advanced Science and Technology, University of Illinois at Urbana-Champaign, Urbana, IL 61801, USA

[3]Thayer School of Engineering, Dartmouth College, Hanover, NH 03755, USA

[4]Département de génie mécanique, Université de Sherbrooke, Sherbrooke, QC J1K 2R1, Canada

[5]Department of Radiology, Dartmouth Hitchcock Medical Center, Lebanon, NH 03756, USA

[6]Norris Cotton Cancer Center, Dartmouth Hitchcock Medical Center, Lebanon, NH 03756, USA

[7]Department of Bioengineering, University of Illinois at Urbana-Champaign, Urbana, IL 61801, USA

Abstract

MRE has been introduced in clinical practice as a possible surrogate for mechanical palpation, but its application to study the human brain in vivo has been limited by low spatial resolution and the complexity of the inverse problem associated with biomechanical property estimation. Here, we report significant improvements in brain MRE data acquisition by reporting images with high spatial resolution and signal-to-noise ratio as quantified by octahedral shear strain metrics. Specifically, we have developed a sequence for brain MRE based on multi-shot, variable-density spiral imaging and three-dimensional displacement acquisition, and implemented a correction scheme for any resulting phase errors. A Rayleigh damped model of brain tissue mechanics was adopted to represent the parenchyma, and was integrated via a finite element-based iterative inversion algorithm. A multi-resolution phantom study demonstrates the need for obtaining high-resolution MRE data when estimating focal mechanical properties. Measurements on three healthy volunteers demonstrate satisfactory resolution of grey and white matter, and mechanical heterogeneities correspond well with white matter histoarchitecture. Together, these advances enable MRE scans that result in high-fidelity, spatially-resolved estimates of in vivo brain tissue mechanical properties, improving upon lower resolution MRE brain studies which only report volume averaged stiffness values.

Keywords

magnetic resonance elastography; brain; high-resolution; multi-shot; spiral; phase error; Rayleigh damping

Address for Correspondence: Curtis L. Johnson, Dept. of Mechanical Science and Engineering, University of Illinois at Urbana-Champaign, 1206 W. Green St., Urbana, IL 61801, cjohns73@illinois.edu.

INTRODUCTION

Magnetic resonance elastography (MRE) is a non-invasive technique for measuring the mechanical properties of tissues in vivo [1] and is potentially of high clinical value as a means of virtual palpation of internal organs. The technique has been used for in vivo probing of the liver, breast, and skeletal muscle [2], and has been introduced into clinical practice as a possible replacement for liver biopsies in the diagnosis of fibrosis [3]. Recently, MRE has been utilized in studies of brain diseases that result in diffuse neurodegeneration such as multiple sclerosis [4,5], normal pressure hydrocephalus [6,7], and Alzheimer's disease [8]. Mechanical properties estimated using MRE and averaged over large regions of the parenchyma have been shown to correlate with the putative degeneration of brain tissue; however, the ability of in vivo MRE to produce accurate local estimates of brain mechanical properties is less well understood. This is primarily due to the mechanical complexity of the brain as an inhomogeneous and anisotropic medium with properties potentially varying between fine tissue structures [9,10], thus high-resolution, full vector field MRE acquisitions in three dimensions with high signal-to-noise ratio (SNR) are required for resolving focal mechanical properties of brain tissue. The need for high spatial resolution in MRE has been recently reinforced by demonstrated local correlations between decrease in viscoelastic properties and demyelination of white matter in a murine model of multiple sclerosis [11].

The role of MR spatial resolution in MRE has not been systematically investigated. In general, high-resolution image acquisitions are necessary for most MRI techniques to reduce partial-volume effects, and thus, allow for delineation of finer features [12,13]. The achievable resolution of MRE is influenced by two factors: spatial resolution and SNR of the displacement data. Small-scale variations in the displacement field caused by fine tissue structures require the acquisition of high-resolution displacement data, and smaller structures will become detectable by the inversion process as resolution improves. In practice, however, MRE displacement images are noisy, and low SNR data requires significant regularization to stabilize the inversion. If the SNR of high-resolution displacements is insufficient, the smoothing effect of the necessary regularization works against the gains achieved by increased resolution. In this sense, we can describe the imaging resolution as "achieved" in a given MRE examination only when there is adequate SNR. In this work, the octahedral shear strain-based SNR (OSS-SNR) measure is used as it has been previously demonstrated that an OSS-SNR of 3.0 will give accurate inversion results [14]. In addition to noise, model-data mismatch also limits the achievable quality of MRE property distributions, as any continuum tissue model is only an approximation of the net effect of enormous numbers of complicated micro-scale interactions. Use of more sophisticated material models can reduce this source of error, however the increase in the number of unknown properties which must be estimated places even more demands on the data, reinforcing the need for high-resolution, high-SNR displacement images. For this work, we adopt a subzone based Non-Linear Inversion (NLI) algorithm [15] and model the tissue as a Rayleigh damped material [16], which has been validated previously in phantoms [17].

In attempting to capture local variations in brain tissue with MRE, the challenge is to develop an MR acquisition scheme that enables high-fidelity MRE data to be obtained during a comfortable and safe subject exam [18,19]. Obtaining high-resolution MRE datasets with adequate SNR relies on the MR sequence used for acquisition. The most common sequences for MRE of the brain are based on single-shot, spin-echo echo-planar imaging (EPI) [20]. EPI-based sequences are attractive because of their rapid acquisition, which keeps examination times short and minimizes subject discomfort. However, in high-resolution protocols, single-shot EPI sequences suffer from very long readout durations.

Long readouts result in large distortions from field inhomogeneity and also require long echo times, thus reducing SNR and ultimately limiting the resolution achievable in a short scan time.

In this work, MRE images with high spatial resolution and adequate SNR are acquired through the implementation of a novel multi-shot, spin-echo sequence with variable-density spiral readout gradients [21,22]. The multi-shot spiral sequence allows easy tradeoffs between resolution, overall acquisition time, and field inhomogeneity distortions, while the self-navigating properties of the variable-density readout allow for correction of any resulting phase errors. In the current work, MRE measurements are performed on phantoms in order to demonstrate the benefits of a high-resolution MRE acquisition, and on three healthy subjects to highlight the potential clinical advantages afforded by the improved scheme. We were able to acquire full-vector field MRE displacement data at an isotropic $2 \times 2 \times 2$ mm^3 resolution on human subjects with an OSS-SNR over 3.0, with a total acquisition time under 10 minutes, well within the limits for safety as proposed by Ehman et al [18]. Though MRE displacement data in the brain has been acquired at the same resolution in other studies [23,24], it is difficult to make comparisons since neither SNR estimates nor conventional MRE inversions are available. In this study, we also adopt an advanced 3D mechanical model and inversion method that has not previously been applied to human brain MRE data, although the sensitivity of the MRE results to model selection and inversion algorithm is beyond the scope of the current investigation.

THEORY

Multi-Shot Spiral Acquisition

Data is acquired in MRE through the incorporation of motion-encoding gradients in MRI sequences for mapping displacement to the phase of the MR signal. Though not always the case [25], these gradients are generally bipolar with period matching to that of the vibration. In brain MRE, which utilizes vibrations in the range of 50–100 Hz, these gradients necessitate the use of long echo times. The most common brain MRE sequence is based on single-shot, spin-echo EPI, which extends the echo time further, especially in high-resolution protocols, due to the symmetric readout gradients. The use of spiral-out readout gradients [26], which have the entire readout after the echo time, enables shorter echo times for a given level of contrast, which is dependent on the total time of the motion-encoding gradients. As no readout gradients are required before the echo time, the spiral sequence allows high-resolution, short echo time acquisitions with echo times that are not dependent on the acquired resolution.

Although spiral readout gradients will accommodate reduced echo times, single-shot sequences still suffer from very long readout times in high-resolution acquisitions. The long readout time can lead to significant distortions in the presence of magnetic field inhomogeneities and susceptibility differences at air-tissue interfaces. These distortions not only degrade the quality of the image, but may also lead to model/data mismatch during the inversion, which produces errors in the resulting estimates of mechanical properties. As an example, geometric distortions from field inhomogeneity can cause compression and stretching of spatial information in certain regions, which can impact the inversion algorithms for determining mechanical properties. Alternatives to single-shot sequences are their multi-shot counterparts, which segment k-space into separately acquired interleaves, or shots. This approach reduces the readout time for each acquisition, and provides access to tradeoffs between acquisition time, resolution, and sensitivity to off-resonance effects and T_2*-induced blurring during readout. It should be noted that the use of parallel imaging could also be used to reduce readout duration, and thus the effects of field inhomogeneity, though with a penalty in SNR that would require averaging to recover.

We have developed an MRE sequence that utilizes multi-shot spiral readout gradients, thus providing high-resolution acquisitions with high SNR and reduced distortions. Specifically, we use 6 shots to acquire a matrix size of 128, giving 2 mm in-plane spatial resolution, with a 15 ms readout duration per shot. The pulse sequence diagram is shown in Figure 1. The motion-encoding gradients are equal in period to the induced vibration (50 Hz for the brain), with the second bipolar gradient pair being placed after the refocusing pulse and one-half period apart [27,28]. Finally, variable-density spiral readout gradients are employed [29], as opposed to constant-density, so that the center of k-space is oversampled with each shot, which ensures that the center of k-space is appropriately captured with each acquisition. It also provides a navigator for motion correction as discussed in the following section.

Correction for Motion-Induced Phase Errors

One drawback of multi-shot imaging in the presence of motion-encoding gradients is the potential for significant phase errors between shots from bulk motion not related to the vibrations of interest. This phase error can lead to phase cancellation and signal loss. Phase error is a well-known phenomenon in diffusion-weighted imaging, where subject motion between the large encoding gradients leads to significant image degradation [30–33]. For an MRE multi-shot sequence, the most likely source of phase error arises from variations in mechanical actuation, which can result from strained mechanical components when loaded with the weight of the head. The applied motion is assumed to be harmonic with constant amplitude; hence, the same motion is mapped to the phase of each shot. However, the output from actuators typically used in MRE does vary in amplitude by a small amount based on their loading, even after reaching an apparent steady-state [34]. Additionally, phase errors may result from brain pulsation since the sequence is not cardiac gated, and also small subject motions not controlled in the experiment.

The majority of accumulated phase in brain MRE is a result of rigid body motion (RBM) – the induced shear waves of interest are diminished in amplitude due to protection of the brain by the skull and cerebrospinal fluid [20]. The amplitude of RBM more closely reflects the applied displacement from the actuator, and thus, any variations can lead to phase errors between shots. In effect, variations in RBM appear as an additional, unwanted RBM phase component, which can be described as a combination of translations and rotations corresponding to bulk phase offsets and linear phase ramps, the latter resulting in k-space trajectory shifts. Anderson and Gore [30] and Van et al. [33] provide a more complete analysis of the effect of RBM phase errors in multi-shot imaging and serve as important references on the topic.

In brief, the measured (and phase corrupted) signal for shot n of a multi-shot image, $\hat{S}^n$ can be described in k-space as (Eq. 1):

$$\widehat{S}^n(k_x^n, k_y^n) = e^{i\Delta\phi^n} \cdot S^n(k_x^n + \Delta k_x^n, k_y^n + \Delta k_y^n). \quad (1)$$

In Eq. 1, S^n is the desired signal for shot n, $\Delta\phi^n$ is the bulk phase offset, k_x^n and k_y^n are the nominal k-space trajectories for shot n, and Δk_x^n and Δk_y^n are the k-space trajectory shifts. As the RBM variations can be different for each shot, all values are defined for a specific shot, n. The corrupted image, $\hat{I}$, is the Fourier transform of the k-space signal summed over all shots (Eq. 2):

$$\widehat{I}(x, y) = \mathscr{F}\{\sum_{n=1}^{N} \widehat{S}^n(k_x^n, k_y^n)\}. \quad (2)$$

In order to recover the uncorrupted image, the phase offsets and k-space shifts need to be estimated for each shot of each image. Estimation was accomplished by using the variable-density spiral readouts as appropriate navigators. To register both k-space shifts and phase offsets for each shot of a specific image, the center of k-space was estimated using the oversampled portion of the spiral readout as the self-navigator, and the k-space center was determined as the sampled point with maximum signal intensity [35] (Eq. 3):

$$\Delta k_x^n, \Delta k_y^n = \arg \max_{k_x^n, k_y^n} |\widehat{S}^n(k_x^n, k_y^n)|. \quad (3)$$

The phase offset for each shot was determined as the phase of the center k-space point (Eq. 4):

$$\Delta \phi^n = \angle \widehat{S}^n(\Delta k_x^n, \Delta k_y^n). \quad (4)$$

Shifts in k-space were corrected by adjusting the k-space trajectory so the center coincided with this same point of maximum signal intensity, and phase offsets were registered between shots by multiplying each shot by the negative of the phase. Applying these corrections to the corrupted signal allowed the uncorrupted signal to be recovered (Eq. 5):

$$\widehat{S}^n(k_x^n - \Delta k_x^n, k_y^n - \Delta k_y^n) \cdot e^{-i\Delta\phi^n} = S^n(k_x^n, k_y^n). \quad (5)$$

Finally, the corrected image, I, is the Fourier transform of the corrected k-space data summed over all shots (Eq. 6):

$$I(x, y) = \mathscr{F}\{\sum_{n=1}^{N} S^n(k_x^n, k_y^n)\}. \quad (6)$$

A schematic depicting the correction steps is given in Figure 2.

Non-Linear Inversion

An NLI algorithm [15,36] was used to produce material property estimates from the measured displacement data. The elastographic inversion is posed as an optimization problem, whereby the function (Eq. 7)

$$\Phi(\theta) = \sum_{i=1}^{N} (u_i^c(\theta) - u_i^m)(u_i^c(\theta) - u_i^m)^* \quad (7)$$

is minimized by iteratively updating the material property description, θ. Here, u_i^m is measured displacement amplitude at location i, $u_i^c(\theta)$ is a computational model of the material behavior (sampled at location i), and the * indicates the complex conjugate. The minimization is performed using the conjugate gradient method, and a numerical solution of most any conceivable mechanical model can be used for $u_i^c(\theta)$. For this study a finite element implementation of a nearly incompressible Rayleigh damped material was used [16,17], where the motion amplitude field, u, was calculated from Navier's equation (Eq. 8)

$$\nabla \cdot \mu(\nabla u + \nabla u^T) + \nabla(\lambda \nabla \cdot u) = \rho \omega^2 u. \quad (8)$$

Here, λ is the first Lamé parameter, μ is the second Lame parameter, or the shear modulus, ρ is the density, and ω is the actuation frequency. In a Rayleigh damped model, both shear modulus and density are complex-valued and account for two mechanisms of damping [17]: the imaginary shear modulus includes damping effects proportional to the elastic forces in the material, and the imaginary density provides damping related to inertial forces. The combination of these two effects may allow better characterization of the micro-scale interactions that cause motion attenuation, compared to the more commonly used viscoelastic model, which does not incorporate inertial damping effects. The material properties estimated during the inversion were the real and imaginary shear modulus, and imaginary part of the density. The real component of the density was set to 1020 kg/m^3, and λ was assumed to be large (10^8 Pa) to model the nearly incompressible behavior expected for fluid saturated tissues such as the brain.

For comparison with MRE results using viscoelastic models, Van Houten et al. [17] also define an effective shear modulus, $\tilde{\mu}$, for an equivalent viscoelastic material (Eq. 9):

$$\tilde{\mu} = \mu \frac{\rho_R}{\rho}. \quad (9)$$

In this equation, μ is the complex-valued Rayleigh shear modulus, ρ_R is the real-valued density of a viscoelastic model, and ρ is the complex-valued counterpart in the Rayleigh model. In homogeneous property regions, a viscoelastic model with a complex-valued shear modulus of $\tilde{\mu}$ is indistinguishable from the Rayleigh model; however, when spatially varying properties are present (as assumed in nearly all tissues), Rayleigh and viscoelastic damping predict different behavior.

METHODS

Phantom experiments were performed to evaluate the impact of spatial resolution in the MRE acquisition scheme we have introduced on the detection of features in the resulting stiffness maps. MRE measurements were also acquired on three healthy volunteers following approval for the study by our Institutional Review Board, and after obtaining written informed consent. Participants were all male, and are identified as subjects A, B, and C (24, 34, and 52 years old, respectively). All scanning was performed using a Siemens 3T Allegra head-only scanner (Siemens Medical Solutions; Erlangen, Germany).

Phantom Experiments

The phantom used in the experiments was a rectangular parallelepiped composed of agarose gel (1%) with three stiffer inclusions (2%) embedded. The inclusions were cubes of three different sizes: 10, 15, and 20 mm on a side. Shear waves were generated by vibrating the lower surface of the phantom at 100 Hz.

Images were acquired using the multi-shot spiral MRE sequence with bipolar motion-encoding gradients matched in period to the vibration frequency of 100 Hz. MRE encoding was performed on each of the three cardinal gradient directions independently, and a single period of vibration was sampled with eight evenly spaced points. Six interleaved spiral shots were used to cover k-space with a 64×64 matrix size for the phantom, with resolution achieved by adjusting the overall field-of-view: 128, 192, and 256 mm. Twenty slices were acquired with 2, 3, or 4 mm thickness, corresponding to the in-plane resolution resulting in isotropic resolutions of 2×2×2, 3×3×3, and 4×4×4 mm^3, respectively. The repetition and echo times for all acquisitions were 2000 ms and 35 ms, respectively.

The NLI inversion process interpolated the displacements to 1.7 mm resolution, providing approximately 16 nodes per wavelength for the finite element forward problem [37]. Interpolation allows a consistent mesh resolution for the finite element computational model used in the inversion regardless of the data resolution. As a result, the quality of the mechanical property images is primarily governed by the acquired data resolution and the ability to capture small variations in the displacement field. The properties were reconstructed at the resolution of the acquired data to hold the ratio of independent measurements to unknowns constant.

In Vivo Brain Experiments

Actuation during the brain MRE experiments was performed with a system that comprised a remote electromagnetic shaker having a long rod that vibrates a custom cradle the subject's head rests on, similar to the one used in other brain MRE studies [20]. The actuator imparts a nodding motion to the head at the driving frequency of 50 Hz. Imaging was performed in the same manner as the phantom studies with motion encoding along three axes and eight samples over a single period. Imaging parameters included: six k-space interleaves; 256 mm field-of-view; 128×128 matrix; 20 axial slices (2 mm thick) in the region of the corpus callosum; 2000/55 ms repetition/echo times. This acquisition resulted in an isotropic resolution of $2\times2\times2$ mm^3 and was repeated with negatively polarized gradients to remove background phase effects and to provide a signal average. Total acquisition time was less than 10 minutes.

Each image was reconstructed using the motion correction procedure described previously. Complex-valued subtraction was used to combine corrected images with positive and negative gradient polarization, and the resulting phase images were unwrapped [38]. Motion at the first harmonic was extracted using a temporal Fourier transform, and the result was a set of 3D complex-valued displacements in three motion directions. No further filtering was applied to the data prior to inversion with the NLI algorithm. To estimate the quality of each acquired MRE dataset, the OSS-SNR was calculated [14].

In addition to MRE, a T_1-weighted MPRAGE scan was acquired for each subject (2000/900/2.2 ms repetition/inversion/echo times; $1\times1\times1$ mm^3 resolution). The MPRAGE data was registered to the MRE acquisition and segmentation of grey matter, white matter, and cerebrospinal fluid was performed using the BET [39], FLIRT [40], and FAST [41] tools in FSL 4.1.9 (FMRIB, www.fmrib.ox.ac.uk/fsl; [42]).

RESULTS

The estimated real shear modulus of the phantom was calculated for each of the three datasets (2, 3, and 4 mm isotropic resolutions), and the resulting distributions are presented in Figure 3 along with a T_2-weighted image clearly depicting the inclusions (cubes of size 10, 15, and 20 mm). The average estimated stiffness of each inclusion, as measured with each resolution, was calculated over regions-of-interest, and are presented in Figure 4.

Though the phantom data did not exhibit significant motion-induced phase errors, such errors were prevalent in the in vivo brain data due to the increased loading of the head on the actuator. The motion-induced phase error correction method provides significantly increased coherence and SNR across shots for in vivo brain data, thus leading to an improvement in the calculated mechanical property distributions, as shown in Figure 5. Signal lost due to phase cancellation is recovered, as seen in the magnitude of the raw MRE images before processing (Figure 5A–B). This signal recovery leads to an improvement in the quality of MRE displacement data (Figure 5C–D) as assessed by OSS-SNR, which is presented for the same slice in Figure 5E–F. The mean OSS-SNR for this dataset before recovery was 3.47

and after recovery was 5.76, demonstrating a gain of 1.66 for this subject. The mean OSS-SNR for each phase-corrected dataset was calculated by averaging over the imaged volume, excluding regions of cerebrospinal fluid, and these results are presented in Table 1. Finally, the real shear modulus distributions calculated from data without and with phase correction are given in Figure 5G–H.

Real shear modulus distributions of all three volunteers are presented in Figure 6 as axial slices with sagittal and coronal reformats around the corpus callosum. For an equivalent estimate of the complex viscoelastic shear modulus, the data was converted using Eq. 9. For each subject, the average real and imaginary parts of the equivalent viscoelastic modulus ($\tilde{\mu}_R$ and $\tilde{\mu}_I$ respectively) were determined for both white matter and grey matter of the cerebral cortex, and the results are presented in Table 1. Also included in Table 1 are values reported in the brain MRE literature [43] for comparison.

DISCUSSION

Phantom Experiments

The need for acquiring MRE data with high spatial resolution is often overlooked when performing studies and quantifying the resulting estimates of mechanical properties. Doyley et al. [44] previously investigated the limits of elastography in detecting and characterizing focal lesions, and determined that both detection and characterization are dependent on lesion size and stiffness. However, the Doyley study was performed at a fixed spatial resolution, and did not consider how the resulting estimates might change with the data acquisition resolution. In this work, we performed a multi-resolution phantom experiment to determine whether spatial resolution of the MRE acquisition played a role in detection and characterization of material inclusions.

The estimates of real shear modulus presented in Figure 3 demonstrate the importance of spatial resolution in MRE. Of the three resolutions investigated – 2, 3, and 4 mm – only data acquired at 2 mm and 3 mm allowed detection of the smallest inclusion, which is 10 mm in size and marked by the arrow in Figure 3. The rectangular shape of the inclusions was also recovered more accurately at higher data resolution. The quantitative characterization of the inclusions also changes with spatial resolution, as the estimated real shear modulus increases with improved resolution and size of the inclusion. The largest inclusion was found to be approximately 18.5 kPa, compared to a 4.0 kPa background, which agrees roughly with expected values from literature, while considering uncertainty due to the sensitivity of agarose shear modulus to thermal history [45–47]. However, this value was found only with the highest resolution, and was not recovered for the other inclusions or other resolutions, as the estimated contrast decreases with both decreasing size and data acquisition resolution (Figure 4). This finding is consistent with Doyley [44], who showed that accurate stiffness characterization of focal inclusions is dependent on size of the heterogeneity.

From the results of the phantom experiment presented in Figures 3 and 4, it is apparent that there is a certain resolution relative to inclusion size needed to accurately recover the true shear modulus of the inclusion. Based on this experiment, we can estimate that approximately ten voxels across the inclusion would be needed for accurate quantification, though without independent mechanical testing to determine the true modulus and a finer range of tested spatial resolutions, it is difficult to pinpoint an exact limit. Additionally, this limit will likely also depend on frequency of actuation, contrast of inclusion modulus with the background, and SNR. In this experiment, all acquisitions had very high SNR (OSS-SNR > 15), and we do not expect noise to have played a role in our results.

In Vivo Brain Experiments

Producing accurate, reliable estimates of the mechanical properties of tissue with NLI algorithms is critically dependent on the quality of the acquired MRE displacement images, with quality being defined here as both adequate spatial resolution and measurement SNR. In this work, we developed an MRE sequence capable of acquiring high-resolution, high-SNR datasets through multi-shot, variable-density spiral readouts. Multi-shot imaging, however, introduces the need to account for phase errors between shots, which result in loss of signal in the MR images as observed in Figure 5A. In MRE, these phase errors can be attributed to variations in the amplitude of motion imparted by the actuator, which effectively contributed an additional, erroneous RBM phase component to the signal. We corrected for these phase errors using a technique well known in diffusion-weighted imaging, which led to a marked increase in image quality (Figure 5B). This correction leads to high-quality MRE displacement data, as visualized in Figure 5D. There is a visible increase in quality over the uncorrected displacement data (Figure 5C), especially in the left/right asymmetry in shear wave pattern.

Improvements in the quality of MRE data can be visualized through the calculated OSS-SNR distributions (Figure 5E–F). Phase errors lead to signal loss in the MR images resulting in an increase in noise in the displacement fields calculated from the phase, and significantly decreasing the OSS-SNR to levels that are below the threshold required for accurate inversion, which is approximately 3.0 [14]. Correction for RBM-induced phase errors results in the recovery of high fidelity displacement data with an improvement in OSS-SNR by a factor of approximately 1.5 across all subjects. In this case, the OSS-SNR value was determined as the average over the imaged volume, though the distribution (in Figure 5F) demonstrates that data with high OSS-SNR is obtained even in the center of the brain where motion is significantly attenuated. The correction for phase errors also improves the resulting shear modulus distributions, shown in Figure 5G–H. The distribution calculated from the uncorrected data demonstrates significant left/right asymmetry compared with the corrected data. Additionally, anatomical features visible in the corrected data are obscured in the uncorrected data.

The mechanical properties of white and cortical grey matter have been reported in several prior MRE studies [43,48,49]. In Table 1, we chose to compare with the values reported by Zhang et al. [43], who also used a 3D mechanical model. It should be noted that the values from Zhang are the averages over eight subjects (aged 22–43 years) of their average white and grey matter moduli, and thus the standard errors of those measures are not directly comparable to the standard errors reported for each of the subject in this study. In general, good agreement occurs for both $\tilde{\mu}_R$ and $\tilde{\mu}_I$ of white matter; however, the $\tilde{\mu}_R$ and $\tilde{\mu}_I$ of grey matter found here are lower than those reported by Zhang, with the difference between white and grey matter reported here being more similar to ex vivo studies [10,50]. The discrepancy in calculated grey matter values may be related to the increased spatial resolution used in this study (2 mm isotropic vs. 3 mm isotropic), allowing for the two tissue types to be better resolved in our case, as demonstrated by the multi-resolution phantom study. Despite improved resolution, the cortex is a very thin structure [51] and it is unlikely that MRE is yet capable of capturing the true shear modulus of cortical grey matter, thus the results presented here must be considered preliminary.

The value of our technique is that it allows brain MRE to capture local variations in the viscoelastic properties of tissue. By obtaining brain MRE data with improved spatial resolution and adequate SNR, we can begin to identify structures in the white matter based on their shear stiffness. Referring to the top row of Figure 6, which shows the real shear modulus on a single slice through the genu and splenium of the corpus callosum for each of the three volunteers, the two ventricles are clearly outlined as soft regions. This is expected

as the ventricles are fluid-filled structures and should exhibit zero shear modulus, though in this case they are modeled along with the tissue as a solid and must have finite stiffness. Qualitatively, the genu of the corpus callosum and the forceps anterior tracts can be identified as stiffer regions in each subject on the axial slice, while the body of the corpus callosum can be identified superior to the ventricles in the sagittal and coronal planes. The importance of spatially resolving the mechanical properties of the corpus callosum became clear by the recent MRE study of the murine model of multiple sclerosis [11]. Additionally, the corticospinal tracts inferior to the corona radiata appear as very stiff regions to the left and right of the ventricles in the axial view, though are not uniform bilaterally. The coronal plane reveals the corona radiata tracts themselves superior to regions of lower stiffness corresponding to grey matter of the lateral sulci.

We have presented qualitative evidence that high-resolution MRE is capable of resolving local variations in tissue stiffness which correlate with the white matter structures in the brain. To our knowledge, no other reports delineating brain structures directly from MRE stiffness maps to this degree have been published. Noteworthy is the recent "waveguide elastography" study by Romano et al. [23], where the corticospinal tracts were first delineated by fiber tracking prior to applying an anisotropic inversion for the evaluation of the elastic parameters. The regional variation of mechanical properties, however, seems to be consistent with the variation of the volume fraction of axons, as demonstrated by Abolfathi et al. [52], who considered the white matter as a composite medium consisting of axons embedded in a matrix. This representation is consistent with the data presented in Figure 6. Indeed, regions with highly oriented axons (corpus callosum, corticospinal tracts, corona radiata) have higher volume fraction of axons and higher viscoelastic values. Future work will look to quantify the mechanical properties of individual structures in the white matter architecture.

CONCLUSIONS

To improve the prospects of magnetic resonance elastography (MRE) as a non-invasive technique for measuring focal mechanical properties of brain tissue in vivo, we have increased the spatial resolution of the method without compromising image acquisition speed or SNR. We have developed and implemented a brain MRE sequence based on multi-shot and variable-density spiral imaging to measure tissue displacement vectors in 3D with high spatial resolution. A Rayleigh damped model of brain tissue mechanics was adopted for the inversion, and was employed via a finite element-based iterative inversion algorithm. Our method was validated on an agarose gel phantom with embedded inclusions and demonstrated that spatial resolution plays a significant role in both detecting and characterizing local variations in viscoelastic properties. MRE measurements on healthy volunteers demonstrate that a plethora of white matter structures can be delineated directly from the MRE stiffness maps. These results set the stage for mechanical property contrast delineation of white matter structures, and future work will investigate the accuracy and repeatability of the quantitative mechanical property measures generated using the MRE data acquisition scheme presented here.

Acknowledgments

References

1. Muthupillai R, Lomas DJ, Rossman PJ, Greenleaf JF, Manduca A, Ehman RL. Magnetic Resonance Elastography by Direct Visualization of Propagating Acoustic Strain Waves. Science. 1995; 269:1854–1857. [PubMed: 7569924]

2. Mariappan YK, Glaser KJ, Ehman RL. Magnetic Resonance Elastography: a Review. Clin Anat. 2010; 23:497–511. [PubMed: 20544947]

3. Yin M, Talwalkar JA, Glaser KJ, Manduca A, Grimm RC, Rossman PJ, Fidler JL, Ehman RL. Assessment of Hepatic Fibrosis with Magnetic Resonance Elastography. Clin Gastroenterol H. 2007; 5:1207–1213.

4. Wuerfel J, Paul F, Beierbach B, Hamhaber U, Klatt D, Papazoglou S, Zipp F, Martus P, Braun J, Sack I. MR-Elastography Reveals Degradation of Tissue Integrity in Multiple Sclerosis. NeuroImage. 2010; 49:2520–2525. [PubMed: 19539039]

5. Streitberger K-J, Sack I, Krefting D, Pfüller C, Braun J, Paul F, Wuerfel J. Brain Viscoelasticity Alteration in Chronic-Progressive Multiple Sclerosis. PLoS One. 2012; 7:e29888. [PubMed: 22276134]

6. Streitberger K-J, Wiener E, Hoffmann J, Freimann FB, Klatt D, Braun J, Lin K, McLaughlin JR, Sprung C, Klingebiel R, Sack I. In Vivo Viscoelastic Properties of the Brain in Normal Pressure Hydrocephalus. NMR Biomed. 2011; 24:385–392. [PubMed: 20931563]

7. Freimann FB, Streitberger K-J, Klatt D, Lin K, McLaughlin JR, Braun J, Sprung C, Sack I. Alteration of Brain Viscoelasticity After Shunt Treatment in Normal Pressure Hydrocephalus. Neuroradiology. 2012; 54:189–196. [PubMed: 21538046]

8. Murphy MC, Huston J III, Jack CR Jr, Glaser KJ, Manduca A, Felmlee JP, Ehman RL. Decreased Brain Stiffness in Alzheimer's Disease Determined by Magnetic Resonance Elastography. J Magn Reson Imaging. 2011; 34:494–498. [PubMed: 21751286]

9. Prange M, Margulies SS. Regional, Directional, and Age-Dependent Properties of the Brain Undergoing Large Deformation. J Biomech Eng-T ASME. 2002; 124:244–252.

10. van Dommelen JAW, van der Sande TPJ, Hrapko M, Peters GWM. Mechanical Properties of Brain Tissue by Indentation: Interregional Variation. J Mech Behav Biomed. 2010; 3:158–166.

11. Schregel K, Wuerfel E, Garteiser P, Gemeinhardt I, Prozorovski T, Aktas O, Merz H, Petersen D, Wuerfel J, Sinkus R. Demyelination Reduces Brain Parenchymal Stiffness Quantified in Vivo by Magnetic Resonance Elastography. P Natl Acad Sci USA. 2012; 109:6650–6655.

12. Karampinos DC, Van AT, Olivero WC, Georgiadis JG, Sutton BP. High-Resolution Diffusion Tensor Imaging of the Human Pons with a Reduced Field-of-View, Multishot, Variable-Density, Spiral Acquisition at 3 T. Magn Reson Med. 2009; 62:1007–1016. [PubMed: 19645009]

13. Pfefferbaum A, Sullivan EV. Increased Brain White Matter Diffusivity in Normal Adult Aging: Relationship to Anisotropy and Partial Voluming. Magn Reson Med. 2003; 49:953–961. [PubMed: 12704779]

14. McGarry MDJ, Van Houten EEW, Perriñez PR, Pattison AJ, Weaver JB, Paulsen KD. An Octahedral Shear Strain-Based Measure of SNR for 3D MR Elastography. Phys Med Biol. 2011; 56:N153–N164. [PubMed: 21654044]

15. Van Houten EEW, Miller MI, Weaver JB, Kennedy FE, Paulsen KD. Three-Dimensional Subzone-Based Reconstruction Algorithm for MR Elastography. Magn Reson Med. 2001; 45:827–837. [PubMed: 11323809]

16. McGarry MDJ, Van Houten EEW. Use of a Rayleigh Damping Model in Elastography. Med Biol Eng Comput. 2008; 46:759–766. [PubMed: 18521645]

17. Van Houten EEW, Viviers DV, McGarry MDJ, Perriñez PR, Perreard IM, Weaver JB, Paulsen KD. Subzone Based Magnetic Resonance Elastography Using a Rayleigh Damped Material Model. Med Phys. 2011; 38:1993–2004. [PubMed: 21626932]

18. Ehman EC, Rossman PJ, Kruse SA, Sahakian AV, Glaser KJ. Vibration Safety Limits for Magnetic Resonance Elastography. Phys Med Biol. 2008; 53:925–935. [PubMed: 18263949]

19. Liu G-R, Gao P-Y, Lin Y, Xue J, Wang X-C, Sui B-B, Ma L, Xi Z-N, Bai Q, Shen H. Brain Magnetic Resonance Elastography on Healthy Volunteers: a Safety Study. Acta Radiol. 2009; 50:423–429. [PubMed: 19241188]

20. Sack I, Beierbach B, Hamhaber U, Klatt D, Braun J. Non-Invasive Measurement of Brain Viscoelasticity Using Magnetic Resonance Elastography. NMR Biomed. 2008; 21:265–271. [PubMed: 17614101]

21. Johnson, CL.; Chen, DD.; Gharibans, AA.; Olivero, WC.; Sutton, BP.; Georgiadis, JG. Interleaved Spiral Sequence for MR Elastography of the Brain. Proceedings of the 19th Annual Meeting of ISMRM; Montreal, Quebec, Canada. 2011. p. 1474

22. Johnson, CL.; McGarry, MDJ.; Gharibans, AA.; Weaver, JB.; Paulsen, KD.; Sutton, BP.; Georgiadis, JG. High-Resolution Multi-Shot MR Elastography of the Brain with Correction for Motion-Induced Phase-Errors. Proceedings of the 20th Annual Meeting of ISMRM; Melbourne, Australia. 2012. p. 2517

23. Romano A, Scheel M, Hirsch S, Braun J, Sack I. In Vivo Waveguide Elastography of White Matter Tracts in the Human Brain. Magn Reson Med. 201210.1002/mrm.24141

24. Papazoglou S, Hirsch S, Braun J, Sack I. Multifrequency Inversion in Magnetic Resonance Elastography. Phys Med Biol. 2012; 57:2329–2346. [PubMed: 22460134]

25. Rump J, Klatt D, Braun J, Warmuth C, Sack I. Fractional Encoding of Harmonic Motions in MR Elastography. Magn Reson Med. 2007; 57:388–395. [PubMed: 17260354]

26. Glover GH. Simple Analytic Spiral K-Space Algorithm. Magn Reson Med. 1999; 42:412–415. [PubMed: 10440968]

27. Sinkus R, Lorenzen J, Schrader D, Lorenzen M, Dargatz M, Holz D. High-Resolution Tensor MR Elastography for Breast Tumour Detection. Phys Med Biol. 2000; 45:1649–1664. [PubMed: 10870716]

28. Sinkus, R.; Weiss, S., inventors. Method of Examing an Object by Means of Elastography U.S. Patent 10/506. p. 456

29. Kim D-H, Adalsteinsson E, Spielman D. Simple Analytic Variable Density Spiral Design. Magn Reson Med. 2003; 50:214–219. [PubMed: 12815699]

30. Anderson AW, Gore JC. Analysis and Correction of Motion Artifacts in Diffusion Weighted Imaging. Magn Reson Med. 1994; 32:379–387. [PubMed: 7984070]

31. Liu C, Bammer R, Kim D, Moseley ME. Self-Navigated Interleaved Spiral (SNAILS): Application to High-Resolution Diffusion Tensor Imaging. Magn Reson Med. 2004; 52:1388–1396. [PubMed: 15562493]

32. Li T, Kim D, Moseley ME. High-Resolution Diffusion-Weighted Imaging with Interleaved Variable-Density Spiral Acquisitions. J Magn Reson Imaging. 2005; 21:468–475. [PubMed: 15779030]

33. Van AT, Karampinos DC, Georgiadis JG, Sutton BP. K-Space and Image-Space Combination for Motion-Induced Phase-Error Correction in Self-Navigated Multicoil Multishot DWI. IEEE T Med Imaging. 2009; 28:1770–1780.

34. Plewes DB, Luginbuhl C, Macgowan CK, Sack I. An Inductive Method to Measure Mechanical Excitation Spectra for MRI Elastography. Concept Magn Reson B. 2004; 21B:32–39.

35. Atkinson D, Porter DA, Hill DL, Calamante F, Connelly A. Sampling and Reconstruction Effects Due to Motion in Diffusion-Weighted Interleaved Echo Planar Imaging. Magn Reson Med. 2000; 44:101–109. [PubMed: 10893527]

36. Van Houten EEW, Paulsen KD, Miller MI, Kennedy FE, Weaver JB. An Overlapping Subzone Technique for MR-Based Elastic Property Reconstruction. Magn Reson Med. 1999; 42:779–786. [PubMed: 10502768]

37. McGarry, MDJ.; Van Houten, EEW.; Johnson, CL.; Sutton, BP.; Georgiadis, JG.; Weaver, JB.; Paulsen, KD. Multi-Resolution Reconstruction of Mechanical Properties using NonLinear Inversion MR Elastography. Proceedings of the 20th Annual Meeting of ISMRM; Melbourne, Australia. 2012. p. 2520

38. Wang H, Weaver JB, Perreard IM, Doyley MM, Paulsen KD. A Three-Dimensional Quality-Guided Phase Unwrapping for MR Elastography. Phys Med Biol. 2011; 56:3935–3952. [PubMed: 21666289]

39. Smith SM. Fast Robust Automated Brain Extraction. Hum Brain Mapp. 2002; 17:143–155. [PubMed: 12391568]

40. Jenkinson M, Smith S. A Global Optimisation Method for Robust Affine Registration of Brain Images. Med Image Anal. 2001; 5:143–156. [PubMed: 11516708]

41. Zhang Y, Brady M, Smith S. Segmentation of Brain MR Images Through a Hidden Markov Random Field Model and the Expectation-Maximization Algorithm. IEEE T Med Imaging. 2001; 20:45–57.

42. Smith SM, Jenkinson M, Woolrich MW, Beckmann CF, Behrens TEJ, Johansen-Berg H, Bannister PR, De Luca M, Drobnjak I, Flitney DE, Niazy RK, Saunders J, Vickers J, Zhang Y, De Stefano N, Brady JM, Matthews PM. Advances in Functional and Structural MR Image Analysis and Implementation as FSL. NeuroImage. 2004; 23:S208–S219. [PubMed: 15501092]

43. Zhang J, Green MA, Sinkus R, Bilston LE. Viscoelastic Properties of Human Cerebellum Using Magnetic Resonance Elastography. J Biomech. 2011; 44:1909–1913. [PubMed: 21565346]

44. Doyley MM, Weaver JB, Van Houten EEW, Kennedy FE, Paulsen KD. Thresholds for Detecting and Characterizing Focal Lesions Using Steady-State MR Elastography. Med Phys. 2003; 30:495–504. [PubMed: 12722801]

45. Sack I, Buntkowsky G, Bernarding J, Braun J. Magnetic Resonance Elastography: a Method for the Noninvasive and Spatially Resolved Observation of Phase Transitions in Gels. J Am Chem Soc. 2001; 123:11087–11088. [PubMed: 11686724]

46. Normand V, Lootens DL, Amici E, Plucknett KP, Aymard P. New Insight Into Agarose Gel Mechanical Properties. Biomacromolecules. 2000; 1:730–738. [PubMed: 11710204]

47. Aymard P, Martin DR, Plucknett K, Foster TJ, Clark AH, Norton IT. Influence of Thermal History on the Structural and Mechanical Properties of Agarose Gels. Biopolymers. 2001; 59:131–144. [PubMed: 11391563]

48. Di Ieva A, Grizzi F, Rognone E, Tse ZTH, Parittotokkaporn T, Rodriguez y Baena F, Tschabitscher M, Matula C, Trattnig S, Rodriguez y Baena R. Magnetic Resonance Elastography: a General Overview of Its Current and Future Applications in Brain Imaging. Neurosurg Rev. 2010; 33:137–145. [PubMed: 20195674]

49. Chatelin S, Constantinesco A, Willinger R. Fifty Years of Brain Tissue Mechanical Testing: From in Vitro to in Vivo Investigations. Biorheology. 2010; 47:255–276. [PubMed: 21403381]

50. Kaster T, Sack I, Samani A. Measurement of the Hyperelastic Properties of Ex Vivo Brain Tissue Slices. J Biomech. 2011; 44:1158–1163. [PubMed: 21329927]

51. Clarkson MJ, Cardoso MJ, Ridgway GR, Modat M, Leung KK, Rohrer JD, Fox NC, Ourselin S. A Comparison of Voxel and Surface Based Cortical Thickness Estimation Methods. NeuroImage. 2011; 57:856–865. [PubMed: 21640841]

52. Abolfathi N, Naik A, Chafi MS, Karami G, Ziejewski M. A Micromechanical Procedure for Modelling the Anisotropic Mechanical Properties of Brain White Matter. Comput Method Biomec. 2009; 12:249–262.
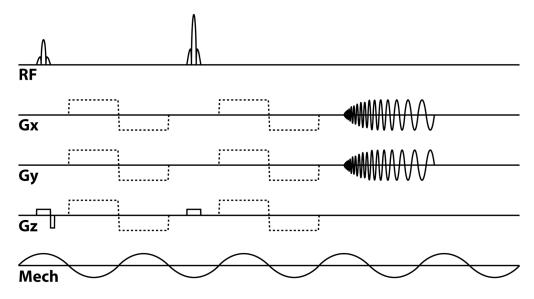
FIG 1.
Diagram of MRE sequence incorporating multi-shot, variable-density spiral readout gradients. Bipolar motion encoding gradients (dashed) are shown on each gradient axis, though are only applied one at a time.

FIG 2.
Schematic depicting correction for RBM-induced phase errors, including phase offsets and k-space trajectory shifts. The center of k-space is determined for each acquired shot as the point with maximum signal amplitude (black dot). Correction is accomplished by shifting the position of the center and applying the negative of the phase to the signal, resulting in the corrected shot and the uncorrupted image. Note that spirals and shifts are greatly exaggerated only for purposes of display.
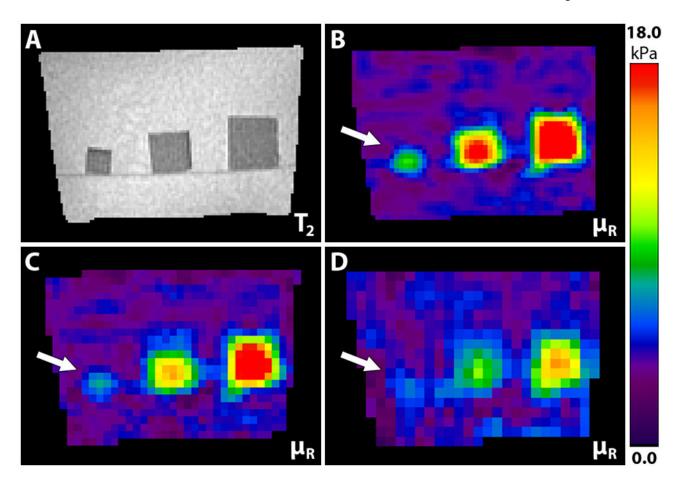
FIG 3.
Calculated real shear modulus distributions for the phantom study. (A) High-resolution T_2-weighted image showing inclusions. Real shear modulus estimates from different isotropic resolutions: (B) 2 mm, (C) 3 mm, and (D) 4 mm. The white arrows show the location of the smallest inclusion.
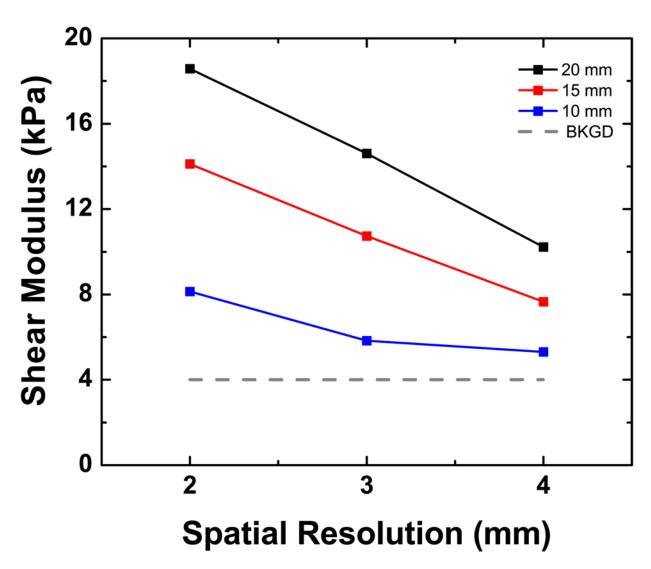
FIG 4.
Calculated real shear moduli of each inclusion compared to background plotted against
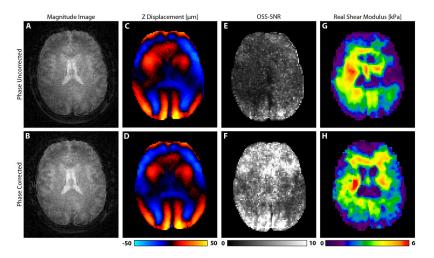isotropic spatial resolution used to obtain displacement data.

FIG 5.
Comparison of MRE data without (top row) and with (bottom row) phase correction: (A and B) magnitude from raw MRE images; (C and D) displacement in the *Z* direction (superior/inferior); (E and F) resulting OSS-SNR distributions; and (G and H) calculated real shear modulus distributions.
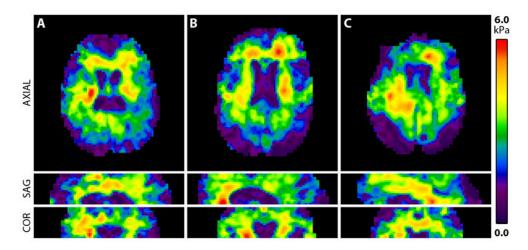
FIG 6.
Axial (top), sagittal (mid), and coronal (bottom) views of real shear modulus distribution from all three volunteers (A, B, and C). Images are presented in radiology convention (subject right is image left; subject anterior is image left in sagittal panel).

TABLE 1

Summary of calculated viscoelastic equivalent shear moduli for each of the three subjects compared to values found by Zhang et al. [43].

Subject		A	B	C	Zhang et al.
Age (years)		24	34	52	Average of eight subjects
OSS-SNR		5.76	3.42	3.82	
White Matter	$\tilde{\mu}_R$ [kPa]	2.49 ± 1.02	2.59 ± 1.05	2.22 ± 1.05	2.41 ± 0.23
	$\tilde{\mu}_I$ [kPa]	1.23 ± 0.75	1.11 ± 0.63	1.29 ± 0.66	1.21 ± 0.21
Grey Matter	$\tilde{\mu}_R$ [kPa]	1.91 ± 0.97	1.82 ± 1.08	1.71 ± 1.02	2.34 ± 0.22
	$\tilde{\mu}_I$ [kPa]	0.79 ± 0.58	0.65 ± 0.49	0.68 ± 0.56	1.11 ± 0.03